FRIEDRICH-ALEXANDER-UNIVERSITÄT ERLANGEN-NÜRNBERG
TECHNISCHE FAKULTÄT • DEPARTMENT INFORMATIK

Lehrstuhl für Informatik 10 (Systemsimulation)

A novel time-domain beam propagation method

Xiao Rao

Masterarbeit

A novel time-domain beam propagation method

Xiao Rao

Masterarbeit

Aufgabensteller:	Prof. Dr. C. Pflaum
Betreuer:	Mr. R. Springer
Bearbeitungszeitraum:	25.09.2018 – 06.07.2019

Erklärung:

Ich versichere, dass ich die Arbeit ohne fremde Hilfe und ohne Benutzung anderer als der angegebenen Quellen angefertigt habe und dass die Arbeit in gleicher oder ähnlicher Form noch keiner anderen Prüfungsbehörde vorgelegen hat und von dieser als Teil einer Prüfungsleistung angenommen wurde. Alle Ausführungen, die wörtlich oder sinngemäß übernommen wurden, sind als solche gekennzeichnet.

Der Universität Erlangen-Nürnberg, vertreten durch den Lehrstuhl für Systemsimulation (Informatik 10), wird für Zwecke der Forschung und Lehre ein einfaches, kostenloses, zeitlich und örtlich unbeschränktes Nutzungsrecht an den Arbeitsergebnissen der Masterarbeit einschließlich etwaiger Schutzrechte und Urheberrechte eingeräumt.

Erlangen, den 06. Juni 2019 .....

Abstract

In this thesis a novel numerical method to simulate beam propagation and pulse amplification is presented, which is based on beam propagation method(BPM) and carries time dependency.

Contents

List of Figures

List of Tables

Chapter 1

Introduction

Chapter 2

Theory

In this chapter, the modified wave equation is derived in the first place, providing an Ansatz for beam propagation in a medium. Combining it with rate equations yields the gain model, allowing amplification by a solid-state medium to be taken into consideration.

2.1 Modified wave equation

Let us start from Maxwell equations in differential form

$$\nabla \times \vec{E} = -\frac{\partial}{\partial t}\vec{B}, \tag{2.1}$$

$$\nabla \times \vec{H} = \frac{\partial}{\partial t}\vec{D} + \vec{J}, \tag{2.2}$$

$$\nabla \cdot \vec{D} = \rho,$$

$$\nabla \cdot \vec{B} = 0,$$

$$\nabla \vec{J} = -\frac{\partial}{\partial t}\rho,$$

along with constitutive equations in medium

$$\vec{D} = \epsilon_0 \vec{E} + \vec{P}, \tag{2.3}$$

$$\vec{H} = \frac{1}{\mu_0}\vec{B} - \vec{M},$$

where displacement filed $\vec{D}$ and magnetizing field $\vec{H}$ are introduced as auxiliary fields, ϵ and μ is the permittivity and permeability in material respectively, with $\vec{P}$ polarization and $\vec{M}$ magnetization.

The following relations hold in material:

$$\vec{D} = \epsilon_r \epsilon_0 \vec{E},$$

$$\vec{B} = \mu_r \mu_0 \vec{H},$$

where ϵ_r and μ_r are relative permittivity and permeability in material, respectively.

Bear in mind that in isotropic linear materials polarization is proportional to electric field and magnetization to $\vec{B}$ in the way

$$\vec{P} = \epsilon_0 \chi_e \vec{E}, \tag{2.4}$$

$$\vec{M} = \chi_m \vec{H}$$

with χ_e and χ_m denoting electric and magnetic susceptibility of material, respectively.

Applying a curl to equation (2.1) and combining it with (2.2) and (2.3) give rise to

$$\nabla \times \nabla \times \vec{E} = -\frac{\partial}{\partial} \nabla \times \vec{B},$$
$$\frac{1}{\epsilon_0}\nabla(\nabla \cdot \vec{P}) + \nabla^2 \vec{E} = \frac{1}{c}\frac{\partial^2 \vec{E}}{\partial t^2} + \mu_0 \frac{\partial^2 \vec{P}}{\partial t^2}. \tag{2.5}$$

Here $c = 1/\epsilon_0\mu_0$ is the speed of light in free space and assumption is taken that there is no current nor magnetism in the material of interest, i.e. $\vec{J} = \vec{0}$, $\mu_r = 1$.

Due to either TE or TM electromagnetic field, it can be concluded that $\nabla(\nabla \cdot \vec{P}) = 0$, which brings equation (2.5) to a simpler expression

$$\nabla^2 \vec{E} = \frac{1}{c}\frac{\partial^2 \vec{E}}{\partial t^2} + \mu_0 \frac{\partial^2 \vec{P}}{\partial t^2}. \tag{2.6}$$

Referring to the relation between polarization and electric field in equation (2.4), one could rewrite vector polarization as follows [1]:

$$\vec{P}(\vec{x}, t) = \epsilon_0 \int_0^{\inf} \chi(\vec{x}, \tau)\vec{E}(\vec{x}, t - \tau)d\tau. \tag{2.7}$$

Then we separate the relatively slowly-varying profile from rapid-changing phase term in the following way

$$\vec{E}(\vec{x}, t) = \vec{e_x} \cdot \Psi(\vec{x}, t)exp(i\omega_0 t) = \vec{e_x} \cdot \psi(\vec{x}, t)exp(i\omega_0 t - i\beta x), \tag{2.8}$$
$$\vec{P}(\vec{x}, t) = \vec{e_x} \cdot \Phi(\vec{x}, t)exp(i\omega_0 t) = \vec{e_x} \cdot \phi(\vec{x}, t)exp(i\omega_0 t - i\beta x), \tag{2.9}$$

where $\vec{e_x}$ is the unit vector in propagation direction, $\beta = k_0\bar{n}$ the propagation constant related to refractive index $\bar{n}$ averaged over space. ψ and ϕ are scalar and complex, denoting profile of electric field and polarization, respectively.

Suppose that $\hat{\chi}(\vec{x}, \omega)$ is the Fourier transform of $\chi(\vec{x}, \tau)$ with frequency ω, inserting equation (2.8) and (2.9) into (2.7) to extract profiles, then expanding $\vec{E}(\vec{x}, t - \tau)$ at $t - \tau = t$ to second order result in

$$\vec{P} = \epsilon_0 \int_{-\inf}^{\inf} \chi(\vec{x}, \tau)\big[\psi(\vec{x}, t) - \frac{\partial}{\partial t}\psi(\vec{x}, t)\tau + \frac{1}{2}\frac{\partial^2}{\partial t^2}\psi(\vec{x}, t)\tau^2\big] \cdot exp(i\omega_0 t - ikx)e_x d\tau,$$
$$\phi = \epsilon_0\hat{\chi}(\vec{x}, \omega)\psi - i\epsilon_0\frac{\partial}{\partial\omega_0}\hat{\chi}(\vec{x}, \omega)\frac{\partial}{\partial t}\psi(\vec{x}, t) - \frac{\epsilon_0}{2}\frac{\partial^2}{\partial\omega_0^2}\hat{\chi}(\vec{x}, \omega)\frac{\partial^2}{\partial t^2}\psi(\vec{x}, t).$$

Neglecting higher-order (over 2) terms, the first and second derivative of polarization could be derived as follows:

$$\begin{aligned}\frac{\partial\Phi(\vec{x}, t)}{\partial t} = &\big[i\epsilon_0\omega_0\hat{\chi}(\vec{x}, \omega)\psi(\vec{x}, t) + \epsilon_0\omega_0\frac{\partial}{\partial\omega_0}\hat{\chi}(\vec{x}, \omega)\frac{\partial}{\partial t}\psi(\vec{x}, t) - i\epsilon_0\frac{\partial}{\partial\omega_0}\hat{\chi}(\vec{x}, \omega)\frac{\partial^2}{\partial t^2}\psi(\vec{x}, t)\\ &- \frac{i\epsilon_0\omega_0}{2}\frac{\partial^2}{\partial\omega_0^2}\hat{\chi}(\vec{x}, \omega)\frac{\partial^2}{\partial t^2}\psi(\vec{x}, t) + \epsilon_0\hat{\chi}(\vec{x}, \omega)\frac{\partial}{\partial t}\psi(\vec{x}, t)\big] \cdot exp(i\omega_0 t - ikz),\end{aligned} \tag{2.10}$$

$$\begin{aligned}\frac{\partial\Phi(\vec{x}, t)}{\partial t^2} = &\big[-\epsilon_0\omega_0^2\hat{\chi}(\vec{x}, \omega)\psi(\vec{x}, t) + i\epsilon_0\omega_0\hat{\chi}(\vec{x}, \omega)\frac{\partial}{\partial t}\psi(\vec{x}, t) + i\epsilon_0\omega_0^2\frac{\partial}{\partial\omega_0}\hat{\chi}(\vec{x}, \omega)\frac{\partial}{\partial t}\psi(\vec{x}, t)\\ &+ \epsilon_0\omega_0\frac{\partial}{\partial\omega_0}\hat{\chi}(\vec{x}, \omega)\frac{\partial^2}{\partial t^2}\psi(\vec{x}, t) + \frac{\epsilon_0\omega_0^2}{2}\frac{\partial^2}{\partial\omega_0^2}\hat{\chi}(\vec{x}, \omega)\frac{\partial^2}{\partial t^2}\psi(\vec{x}, t) + i\epsilon_0\omega_0\hat{\chi}(\vec{x}, \omega)\frac{\partial}{\partial t}\psi(\vec{x}, t)\\ &+ \epsilon_0\omega_0\frac{\partial}{\partial\omega_0}\hat{\chi}(\vec{x}, \omega)\frac{\partial^2}{\partial t^2}\psi(\vec{x}, t) + \epsilon_0\hat{\chi}(\vec{x}, \omega)\frac{\partial^2}{\partial t^2}\psi(\vec{x}, t)\big] \cdot exp(i\omega_0 t - ikz).\end{aligned} \tag{2.11}$$

Inserting above equations (2.10) and (2.11) into (2.6) yield

$$\begin{aligned}\nabla^2\Psi(\vec{x},t) = &-\frac{\omega_0^2}{c^2}\Psi(\vec{x},t) + \frac{2i\omega_0}{c^2}\frac{\partial}{\partial t}\Psi(\vec{x},t) + \frac{i\omega_0}{c^2}\big(2\hat{\chi}(\vec{x},\omega) + \omega_0\frac{\partial}{\partial\omega_0}\hat{\chi}(\vec{x},\omega)\big)\frac{\partial}{\partial t}\Psi(\vec{x},t)\\ &- \frac{\omega_0^2}{c^2}\hat{\chi}(\vec{x},\omega)\Psi(\vec{x},t) + \frac{1}{c}\frac{\partial^2}{\partial t^2}\Psi(\vec{x},t) + \mu_0\epsilon_0\hat{\chi}(\vec{x},\omega)\frac{\partial^2}{\partial t^2}\Psi(\vec{x},t) + \mu_0\frac{\partial^2}{\partial t^2}\Psi(\vec{x},t)\\ &\cdot\big(\frac{\epsilon_0\omega_0^2}{2}\frac{\partial^2}{\partial\omega_0^2}\hat{\chi}(\vec{x},\omega) + 2\epsilon_0\omega_0\frac{\partial}{\partial\omega_0}\hat{\chi}(\vec{x},\omega)\big).\end{aligned}$$

Also, we assume that $\hat{\chi}$ variates little in space for consistency with neglect of second-derivatives. To reach a simpler formulation, the following variables are introduced:

$$\begin{aligned} n_g &= n_R + \omega_0 \cdot \frac{\partial n_R(\omega)}{\partial\omega}|_{\omega=\omega_0}, && \text{group refractive index}\\ n_R &= \sqrt{1+\bar{\chi}}, && \text{real refractive index}\end{aligned}$$

where $\bar{\chi}$ describes average real susceptibility in medium and $c = 1/\sqrt{\mu_0\epsilon_0}$ the speed of light in free space. The equation above could be formulated as

$$\nabla^2\Psi(\vec{x},t) = \frac{\epsilon_r}{c^2}\frac{\partial^2\Psi}{\partial t^2} + 2ik_0\frac{n_R n_g}{c}\frac{\partial}{\partial t}\Psi(\vec{x},t) - k_0^2\epsilon_r\Psi(\vec{x},t), \tag{2.12}$$

where $k_0 = \omega_0/c$ is the wave number in free space and $\epsilon_r = 1+\chi = n^2$ relative permittivity in medium.

If three-dimensional space is considered and wave is assumed to propagate in z direction, Laplace operator can be written as

$$\begin{aligned}\nabla^2 &= \nabla_\perp^2 + \frac{\partial^2}{\partial z^2},\\ \nabla_\perp^2 &= \frac{\partial^2}{\partial x^2} + \frac{\partial^2}{\partial y^2}.\end{aligned}$$

Paraxial approximation is made that electric field ψ has relatively slow z dependency so that its second derivative satisfies [2]

$$|\frac{\partial^2\psi}{\partial z^2}| \ll |\frac{\partial^2\psi}{\partial x^2}|, |\frac{\partial^2\psi}{\partial y^2}|.$$

Thus the equation (2.12) could be further modified into the Ansatz

$$\frac{\epsilon_r}{c^2}\frac{\partial^2\psi}{\partial t^2} + 2ik_0\frac{n_R n_g}{c}\frac{\partial\psi}{\partial t} = \nabla_\perp^2\psi - 2i\beta\frac{\partial\psi}{\partial z} - (\beta^2 - k_0^2\epsilon_r)\psi. \tag{2.13}$$

2.2 Gain model

The formula (2.13) reveals temporal and spatial dependency of waveform, describing evolution of pulse envelope inside a medium. We should note that propagation constant β and refractive index play a significant role relating to absorption and amplification of waves, which is of great essence to build a gain model based on wave and rate equations.

To start with, we consider the transport equations [3] with stimulated and spontaneous emission neglected

$$\begin{aligned}\frac{\partial\Phi}{\partial t} &= c\Delta\sigma\Phi - \frac{\partial\Phi}{\partial x}c\\ \frac{\partial\Delta}{\partial t} &= -2\Delta c_0\sigma n,\end{aligned}$$

where c denotes the speed of light in medium, c_0 the speed of light in free space, σ the cross section, $\Delta = N_2 - N_1$ the population inversion and Φ the photon density.

When loss and gain are included in the model, the wave number will no longer be merely real, so we rewrite k as

$$k = k_0\bar{n} + ik_I = k_0\bar{n} + ik_0 n_I \tag{2.14}$$

The gain of intensity after single pass could be expressed from temporal perspective [2, 4] (7.39) :

$$g_t = exp(2k_I L) \tag{2.15}$$

Besides, the gain could be acquired from the respect of intensity (spatial perspective)

$$g_s = exp(\sigma_e \Delta L). \tag{2.16}$$

Comparing the two equations (2.15) and (2.16) one could easily extract imaginary part of wave number

$$k_I = \frac{\sigma_e \Delta}{2} \tag{2.17}$$

and write the square of wave number referring to (2.14)

$$\begin{aligned} k^2 = k_0^2\epsilon_r &= (k_0\bar{n} + ik_I)^2 \\ &= k_0^2\bar{n}^2 - \frac{\sigma_e^2\Delta^2}{4} + ik_0\bar{n}\sigma_e\Delta. \end{aligned} \tag{2.18}$$

To incorporate electric field into the rate equations, we would make use of the relationships [5] (E.1.2) between stimulated emission rate W_e and energy density ρ [4] in the way

$$\begin{aligned} W_e &= \frac{c_0\sigma_e}{nhv}\rho, \\ \rho &= \frac{n^2\epsilon_0|\psi|^2}{2}, \\ \mapsto W_e &= \frac{\sigma_e c_0 n\epsilon_0}{2\hbar\omega}|\psi|^2 = \frac{\sigma_e\epsilon_0}{2\hbar k_0}|\psi|^2, \end{aligned} \tag{2.19}$$

which is then embedded in the rate equation of 4-level system [5](E.1.1a)

$$\frac{\partial\Delta}{\partial t} = R_p - W_e\Delta - \frac{\Delta}{\tau_f}. \tag{2.20}$$

Here R_p indicates the pumping rate and τ_f the fluorescent lifetime.

Combining equation (2.13) and (2.18) allows to update E-filed ψ, while incorporating the expression (2.19) into (2.20) to update population inversion. Consequently, the equation set of gain model is written as follows

$$\begin{aligned} &\frac{(\bar{n} + \frac{\sigma_e\Delta}{2k_0})^2}{c_0^2}\frac{\partial^2\psi}{\partial t^2} + 2ik_0\frac{\bar{n}n_g}{c_0}\frac{\partial\psi}{\partial t} = \nabla_\perp^2\psi - 2i\beta\frac{\partial\psi}{\partial z} - (\beta^2 - k_0^2(\bar{n} + \frac{\sigma_e\Delta}{2k_0})^2)\psi \\ &\frac{\partial\Delta}{\partial t} = R_p - \frac{\sigma_e\epsilon_0}{2\hbar k_0}|\psi|^2\Delta - \frac{\Delta}{\tau_f} \end{aligned} \tag{2.21}$$

To give a better understanding of the updating procedure, a flow chart 2.1 is presented below.

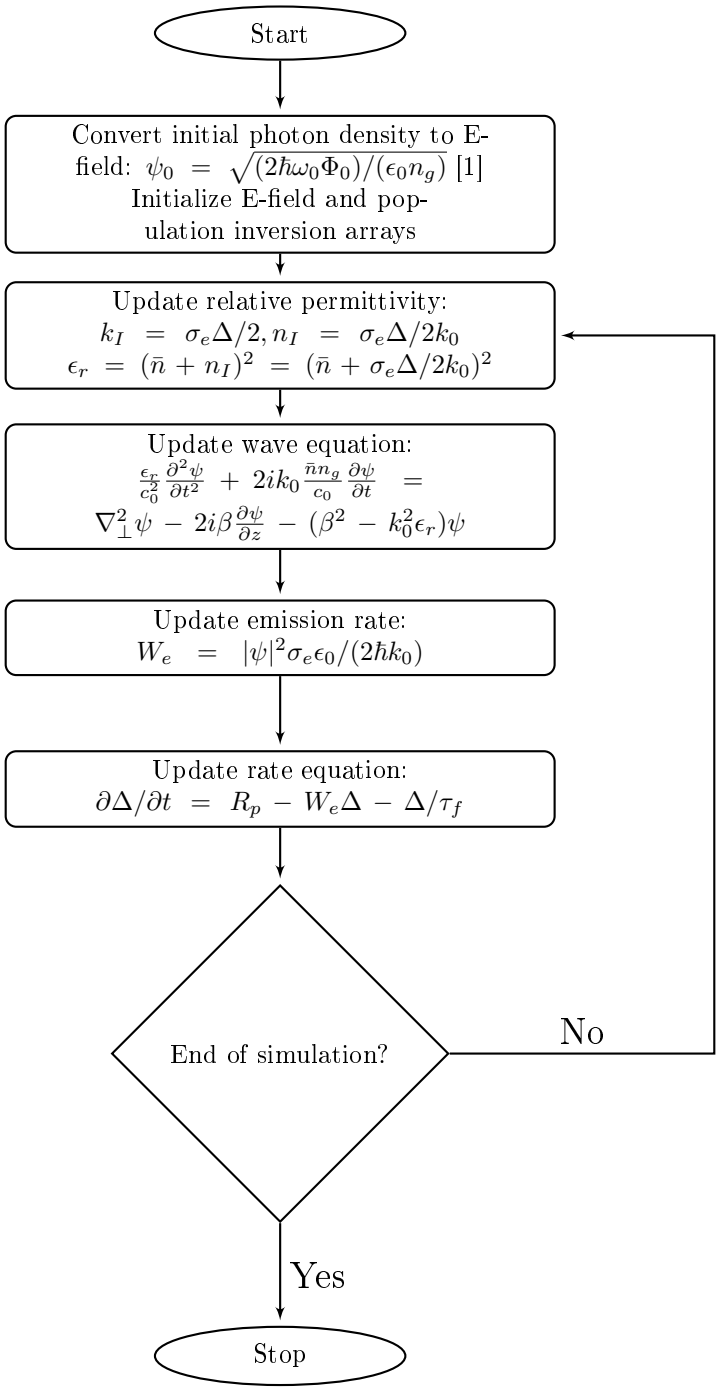

Figure 2.1: The gain is introduced through ϵ_r, which here contains population inversion.

Chapter 3

Model description

In Chapter 2 the formulation of beam propagation and gain model is presented in detail, offering a possibility to find numerical solution of electric field. To do so, a mesh in time and space is introduced, with the following relation between temporal and spatial spacings in propagation direction:

$$\Delta z = \Delta t \cdot \frac{c}{n}. \tag{3.1}$$

Different discretization of partial differential equations (PDEs) leads to distinctive stencils to be implemented upon the mesh.

In this chapter, numerical techniques are built by discretizing modified wave equation and its combination with rate equations.

3.1 Discretization for beam propagation

A natural discretization follows the way by substituting central finite-difference approximation

$$\begin{aligned}
\frac{\partial^2\psi}{\partial t^2} &\approx \frac{1}{\Delta t^2}(\psi^{t+\Delta t}_{x,y,z+\Delta z} + \psi^{t-\Delta t}_{x,y,z+\Delta z} - 2\psi^{t}_{x,y,z+\Delta z}),\\
\frac{\partial\psi}{\partial t} &\approx \frac{1}{2\Delta t}(\psi^{t+\Delta t}_{x,y,z+\Delta z} - \psi^{t-\Delta t}_{x,y,z+\Delta z}), &(3.2)\\
\frac{\partial\psi}{\partial z} &\approx \frac{1}{2\Delta z}(\psi^{t}_{x,y,z+\Delta z} - \psi^{t}_{x,y,z-\Delta z}), &(3.3)\\
\nabla^2_\perp\psi &\approx \frac{1}{\Delta x^2}(\psi^{t}_{x+\Delta x,y,z} + \psi^{t}_{x-\Delta x,y,z} - 2\psi^{t}_{x,y,z}) + \frac{1}{\Delta y^2}(\psi^{t}_{x,y+\Delta y,z} + \psi^{t}_{x,y-\Delta y,z} - 2\psi^{t}_{x,y,z}); &(3.4)
\end{aligned}$$

for partial derivatives in the equation (2.13), which leads to

$$\begin{aligned}
\psi^{t+\Delta t}_{x,y,z+\Delta z} = f_a \cdot \big[& f_b \cdot \psi^{t}_{x,y,z+\Delta z} + f_c \cdot \psi^{t-\Delta t}_{x,y,z+\Delta z} + f_d \cdot \psi^{t}_{x,y,z-\Delta z} + f_e \cdot \psi^{t}_{x,y,z}\\
& + \frac{1}{\Delta x^2}(\psi^{t}_{x+\Delta x,y,z} + \psi^{t}_{x-\Delta x,y,z}) + \frac{1}{\Delta y^2}(\psi^{t}_{x,y+\Delta y,z} + \psi^{t}_{x,y-\Delta y,z})\big]
\end{aligned} \tag{3.5}$$

with

$$\begin{aligned}
f_a &= (\frac{i\omega_0}{\Delta t c^2}\bar{n}n_g + \frac{\epsilon_r}{c^2\Delta t^2})^{-1}, \qquad & f_b &= \frac{2\epsilon_r}{c^2\Delta t^2} - \frac{ik}{\Delta z}, & f_c &= \frac{i\omega_0}{\Delta t c^2}\bar{n}n_g - \frac{\epsilon_r}{c^2\Delta t^2},\\
f_d &= \frac{ik}{\Delta z}, & f_e &= -(k^2 - k_0^2\epsilon_r + \frac{2}{\Delta x^2} + \frac{2}{\Delta y^2}).
\end{aligned}$$

It corresponds to a stencil illustrated by the following scheme 3.1.

However, this stencil cannot work in that the unknown array ψ^t gets updated faster than the marching speed of time steps. The problem is attributed to the variable ψ^t_{z-1}, which stands two steps behind the

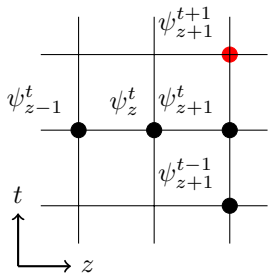

Figure 3.1: This stencil fails to establish simulation as updates proceed too fast. Illustration of one way to discretize modified wave equation. Horizontal axis indicates z direction, i.e. propagation direction of wave front while vertical axis temporal order. To find the solution ψ_{z+1}^{t+1}(marked by the red dot in full color or lighter dot in grayscale), other variables that are marked by black dots are required.

solution of current stencil unit, ψ_{z+1}^{t+1}, in space yet only one step behind in time, contributing to update of ψ_{z+2}^{t+1} thus making solution to proceed faster.

To fix the speed error, we rewrite the ordinary differential equations in such a way

$$\frac{d\psi}{dz} = \frac{\partial\psi}{\partial z} + \frac{n}{c}\frac{\partial}{\partial t}$$

so that equation (3.3) becomes

$$\frac{\partial\psi}{\partial z} \approx \frac{1}{2\Delta z}(\psi_{x,y,z+\Delta z}^{t+\Delta t} - \psi_{x,y,z-\Delta z}^{t-\Delta t})$$

and (3.2)

$$\frac{\partial\psi}{\partial t} \approx (1 - \frac{n}{c})\frac{1}{2\Delta t}(\psi_{x,y,z+\Delta z}^{t+\Delta t} - \psi_{x,y,z+\Delta z}^{t-\Delta t}).$$

This holds as one can refer to mesh establihshment described by equation (3.1).

As a consequence, the discretization is formulated as

$$\begin{aligned}\psi_{x,y,z+\Delta z}^{t+\Delta t} = f_a \cdot [f_b \cdot \psi_{x,y,z+\Delta z}^{t} + f_c \cdot \psi_{x,y,z}^{t} + f_d \cdot \psi_{x,y,z+\Delta z}^{t-\Delta t} + f_e \cdot \psi_{x,y,z-\Delta z}^{t-\Delta t} \\ + \frac{1}{\Delta x^2}(\psi_{x+\Delta x,y,z}^{t} + \psi_{x-\Delta x,y,z}^{t}) + \frac{1}{\Delta y^2}(\psi_{x,y+\Delta y,z}^{t} + \psi_{x,y-\Delta y,z}^{t})]\end{aligned} \tag{3.6}$$

where

$$f_a = (\frac{\epsilon_r}{c^2\Delta t^2} + \frac{ik_0\bar{n}}{\Delta z})^{-1}, \qquad f_b = \frac{2\epsilon_r}{c^2\Delta t^2}$$
$$f_c = -(\beta^2 - k_0^2\epsilon_r) - \frac{2}{\Delta x^2} - \frac{2}{\Delta y^2}, \qquad f_d = -\frac{\epsilon_r}{c^2\Delta t^2}, \qquad f_e = \frac{ik_0\bar{n}}{\Delta z}.$$

Figure 3.2 demonstrates the corresponding stencil. It is noted that now variable ψ_{z-1}^{t-1} is demanded for solution while ψ_{z-1}^{t} not any more, which is the farthest point of each stencil unit in space as well as in time.

If we bring a small modification to the stencil above, wherein equation (3.3) is reconstructed in the way

$$\frac{\partial\psi}{\partial z} \approx \frac{1}{\Delta z}(\psi_{x,y,z+\Delta z}^{t+\Delta t} - \psi_{x,y,z}^{t}) - \frac{\bar{n}}{c\Delta t}(\psi_{x,y,z}^{t+\Delta t} - \psi_{x,y,z}^{t})$$

and we have

$$\frac{\partial\psi}{\partial t} \approx \frac{1}{\Delta t}(\psi_{x,y,z}^{t+\Delta t} - \psi_{x,y,z}^{t}).$$

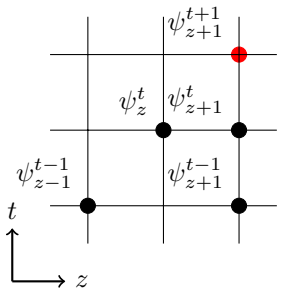

Figure 3.2: The scheme of practical stencil 1. A notable distinction compared to previous stencil is found at the left corner, where the point ψ_{z-1}^{t-1} is demanded instead of ψ_{z-1}^{t}.

Accordingly the complete solution would be

$$\begin{aligned}\psi_{x,y,z+\Delta z}^{t+\Delta t} = f_a \cdot \big[& f_b \cdot \psi_{x,y,z+\Delta z}^{t} + f_c \cdot \psi_{x,y,z}^{t} + f_d \cdot \psi_{x,y,z+\Delta z}^{t-\Delta t} \\ & + \frac{1}{\Delta x^2}(\psi_{x+\Delta x,y,z}^{t} + \psi_{x-\Delta x,y,z}^{t}) + \frac{1}{\Delta y^2}(\psi_{x,y+\Delta y,z}^{t} + \psi_{x,y-\Delta y,z}^{t}) \big]\end{aligned} \tag{3.7}$$

with

$$f_a = (2ik_0\bar{n}\frac{1}{\Delta z} + \frac{\epsilon_r}{c^2\Delta t^2})^{-1}, \qquad f_b = \frac{2\epsilon_r}{c^2\Delta t^2} - \frac{1}{2}(\beta^2 - k_0^2\epsilon_r),$$
$$f_c = 2ik_0\bar{n}\frac{1}{\Delta z} - \frac{1}{2}(\beta^2 - k_0^2\epsilon_r) - \frac{2}{\Delta x^2} - \frac{2}{\Delta y^2}, \qquad f_d = -\frac{\epsilon_r}{c^2\Delta t^2}$$

.

The related scheme is graphed in figure 3.3. This discretization reduces the number of variables required for solution by one. To avoid confusion of these two stencils, we simply call them by stencil 1 and 2, respectively.

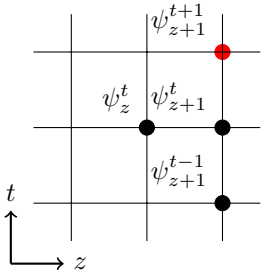

Figure 3.3: The scheme of practicable stencil 2. It is evident that only three variables are needed for solution now.

3.2 Discretization for gain model

Assume that there is no pump and the fluorescent life time is infinite, i.e.

$$R_p = 0,$$
$$\frac{1}{\tau_f} = 0,$$

we apply explicit discretization over equation (2.20) and combine it with forward difference approximation $\partial\Delta/\partial t \approx \Delta^{n+1} - \Delta^n/\Delta t$, which leads to

$$\begin{aligned}\frac{\Delta^{t+1}_{x,y,z+1} - \Delta^{t}_{x,y,z+1}}{\Delta t} &= -\frac{\sigma_e \epsilon_0}{2\hbar k_0}|\psi^{t+1}_{x,y,z+1}|^2 \Delta^{t+1}_{x,y,z+1}, \\ \Delta^{t+1}_{x,y,z+1} &= \frac{\Delta^{t}_{x,y,z+1}}{1 + \frac{\sigma_e \epsilon_0}{2\hbar k_0}|\psi^{t+1}_{x,y,z+1}|^2 \Delta t}\end{aligned} \tag{3.8}$$

By integrating population in (2.13) and employing the variations of discretization discussed in the previous chapter, we obtain the other half for our gain model. For (figure 3.2) stencil 1 its corresponding solution is

$$\begin{aligned}\Delta^{t+1}_{x,y,z+1} &= \frac{\Delta^{t}_{x,y,z+1}}{1 + \frac{\sigma_e \epsilon_0}{2\hbar k_0}|\psi^{t+1}_{x,y,z+1}|^2 \Delta t}, \\ \psi^{t+\Delta t}_{x,y,z+\Delta z} &= f_a \cdot \big[f_b \cdot \psi^{t}_{x,y,z+\Delta z} + f_c \cdot \psi^{t}_{x,y,z} + f_d \cdot \psi^{t-\Delta t}_{x,y,z+\Delta z} + f_e \cdot \psi^{t-\Delta t}_{x,y,z-\Delta z} \\ &\quad + \frac{1}{\Delta x^2}(\psi^{t}_{x+\Delta x,y,z} + \psi^{t}_{x-\Delta x,y,z}) + \frac{1}{\Delta y^2}(\psi^{t}_{x,y+\Delta y,z} + \psi^{t}_{x,y-\Delta y,z})\big]\end{aligned} \tag{3.9}$$

with

$$f_a = \Big(\frac{(\bar{n} + \frac{\sigma_e \Delta^t_z}{2k_0})^2}{c^2 \Delta t^2} + \frac{i k_0 \bar{n}}{\Delta z}\Big)^{-1}. \qquad f_b = \frac{2(\bar{n} + \frac{\sigma_e \Delta^t_z}{2k_0})^2}{c^2 \Delta t^2},$$

$$f_c = -\big(\beta^2 - k_0^2(\bar{n} + \frac{\sigma_e \Delta^t_z}{2k_0})^2\big) - \frac{2}{\Delta x^2} - \frac{2}{\Delta y^2}, \qquad f_d = -\frac{(\bar{n} + \frac{\sigma_e \Delta^t_z}{2k_0})^2}{c^2 \Delta t^2}, \qquad f_e = \frac{i k_0 \bar{n}}{\Delta z}.$$

Figure 3.4 shows stencil 1 for gain model. Here solid dots represent electric field while crosses population inversion. Red-colored marks indicate the unknown while black-colored the known variables.

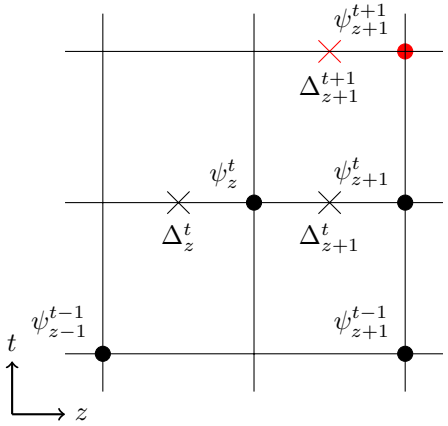

Figure 3.4: Scheme for stencil 1 of gain model.

As for stencil 2 (figure 3.3), analogous incorporation yields the following equation sets:

$$\begin{aligned}\psi^{t+\Delta t}_{x,y,z+\Delta z} &= f_a \cdot \big[f_b \cdot \psi^{t}_{x,y,z+\Delta z} + f_c \cdot \psi^{t}_{x,y,z} + f_d \cdot \psi^{t-\Delta t}_{x,y,z+\Delta z} \\ &\quad + \frac{1}{\Delta x^2}(\psi^{t}_{x+\Delta x,y,z} + \psi^{t}_{x-\Delta x,y,z}) + \frac{1}{\Delta y^2}(\psi^{t}_{x,y+\Delta y,z} + \psi^{t}_{x,y-\Delta y,z})\big]\end{aligned} \tag{3.10}$$

with coefficients

$$f_a = (2ik_0\bar{n}\frac{1}{\Delta z} + \frac{(\bar{n} + \frac{\sigma_e \Delta_z^t}{2k_0})^2}{c^2\Delta t^2})^{-1}, \qquad f_b = \frac{2(\bar{n} + \frac{\sigma_e \Delta_z^t}{2k_0})^2}{c^2\Delta t^2} - \frac{1}{2}(\beta^2 - k_0^2(\bar{n} + \frac{\sigma_e \Delta_z^t}{2k_0})^2),$$

$$f_c = 2ik_0\bar{n}\frac{1}{\Delta z} - \frac{1}{2}(\beta^2 - k_0^2(\bar{n} + \frac{\sigma_e \Delta_z^t}{2k_0})^2) - \frac{2}{\Delta x^2} - \frac{2}{\Delta y^2}, \quad f_d = -\frac{(\bar{n} + \frac{\sigma_e \Delta_z^t}{2k_0})^2}{c^2\Delta t^2}.$$

Figure 3.5 demonstrates the grid points accessed.

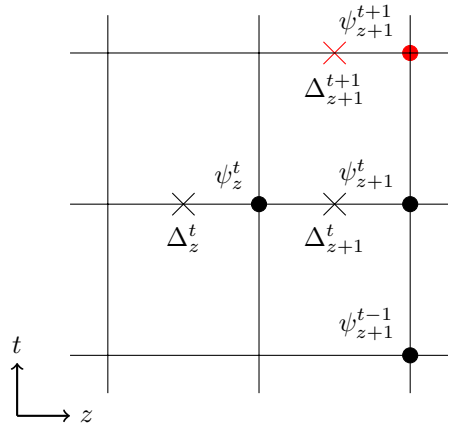

Figure 3.5: Scheme for stencil 2 of gain model.

Chapter 4

Results and discussion

4.1 Convergence tests

Before starting simulation with parameters, the models described in previous chapter need to be validated. A limited simulation regime is made to observe evolution of certain continuous gaussian wave after it reaches the end of regime and stabilizes. The reason to choose such input is that analytic solution with characteristic variables can be directly given and that the temporal continuity eliminates time dependency, making implementation much easier.

The calculation of two models are compared with results given by theoretical formula. The difference between numerical and analytic distribution of electromagnetic waves is taken as error, which serves to quantify accuracy of two models with respect to convergence.

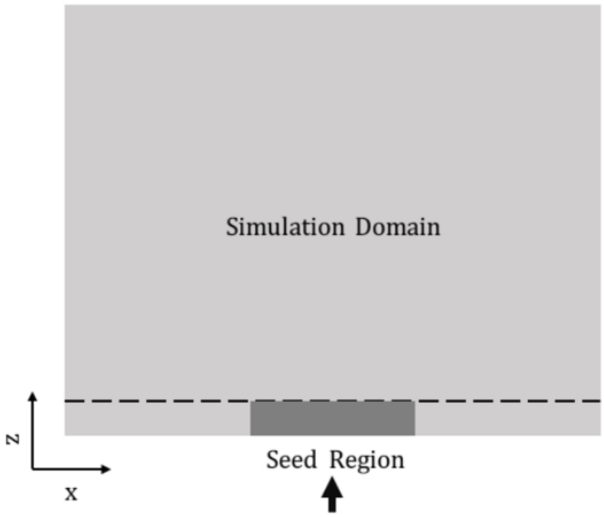

Figure 4.1: An illustration of a gaussian beam in free space.

Figure 4.1 provides a scheme of simulation domain and position of input to be injected. One should note that simulation domain is introduced for convenience of calculation and such a confinement do not exist in practice. During calculation we will inevitably be confronted with boundary problem, i.e. how to deal with values out of simulation regime. In this project we implement Dirichlet boundary condition, demonstrated by the equation (4.1).

$$|\psi| = 0, \qquad \text{if out of boundary} \tag{4.1}$$

Observing the expression above, one may notice the artifact brought by Dirichlet boundary condition, i.e. reflection at either lateral boundary. The assumption that all the outer values are zero indicates no electromagnetic waves out of simulation regime, which is a consequence of complete reflection at incident point of boundary. We observe that defects caused by side reflection increase and worsen with finer mesh and shorter time intervals. To compensate for such an artifact, simulation regime get extended in lateral direction proportionally to mesh size. That is, if mesh size decreases by half, width of simulation regime becomes twofold, fourfold and eightfold of the initial, while length of it keeps constant.

Table 4.1 lists parameters that define initial size of simulation domain and that concerning gaussian waves as input. For 2D models is to be established, propagation direction is assumed at z while lateral at x axis. Three varying mesh sizes are introduced: 5 μm, 2.5 μm and 1.25 μm. The width of simulation regime is set initially as 100 μm.

Table 4.1: Parameters applied in convergence tests

Description	**Symbol**	**Value**	**Units**
Length of simulation domain	L	100	μm
Initial Width of simulation domain	L_x	100	μm
Real refractive index	n_R	1.823	
Group refractive index	n_g	1.823	
Wavelength in free-space	λ_0	1	μm
Simulation duration	T	20	ps
Spot size of gaussian beams at origin	w_0	2.5	μm

To measure error of calculation of two models, we take sum of electric amplitude in the whole simulation regime, and calculate Euclidean and maximum norm to analytic sum, as equation (4.2) and (4.3) describe.

$$\| x \|_2 = \sqrt{\frac{\sum_{x,z}(|\vec{E}|_{numerical} - |\vec{E}|_{analytic})^2}{\text{Number of Grid Points}}} \tag{4.2}$$

$$\| x \|_\infty = \left| (|\vec{E}|_{numerical} - |\vec{E}|_{analytic}) \right|_{max} \tag{4.3}$$

Figure 4.2 illustrates how the two models perform when mesh size varies, with simulation regime extended laterally distinctively. It can be concluded that in general, as mesh sizes drops, deviation of numerical results from theoretical ones decreases as well. Though the difference of Euclidean norm of two models is small referring to (a), stencil 2 gives better precision, or smaller deviation from analytic solutions, compared to the results of stencil 1. Width of simulation regime that is extended by eightfold when mesh size drops by half achieves smaller deviation than being extended by two- and fourfold, with error lines for both models lies below the second-order guide line. Yet generally $\| x \|_\infty$ is larger than $\| x \|_2$. It can be explained that $\| x \|_\infty$ depends only on the maximum of error while $\| x \|_2$ takes an average of error over propagation axis.

In summary, solutions of two numerical models can converge to theoretical results when mesh grid becomes finer, as two types of norm to analytic solution diminishes with smaller mesh size.

4.2 Simulation of gaussian beam propagation in ducts

For insight into evolution of different wavefronts, more scenarios are of interest and to be investigated in the following part. Firstly research concerning propagation of gaussian beams is conducted. The simpler case, where wave passes through medium with constant refractive index (RI), has been calculated in convergence tests. A more interesting circumstance deals with varying RI distributed central symmetrically.

To begin with, let us have a look at propagation of gaussian beams in homogeneous medium. Consider a coordinate where a gaussian beam propagates along its positive z axis. The wave's spot size at $z = 0$, aka beam waist, is denoted by w_0. A conventional expression of gaussian spherical wave is written as

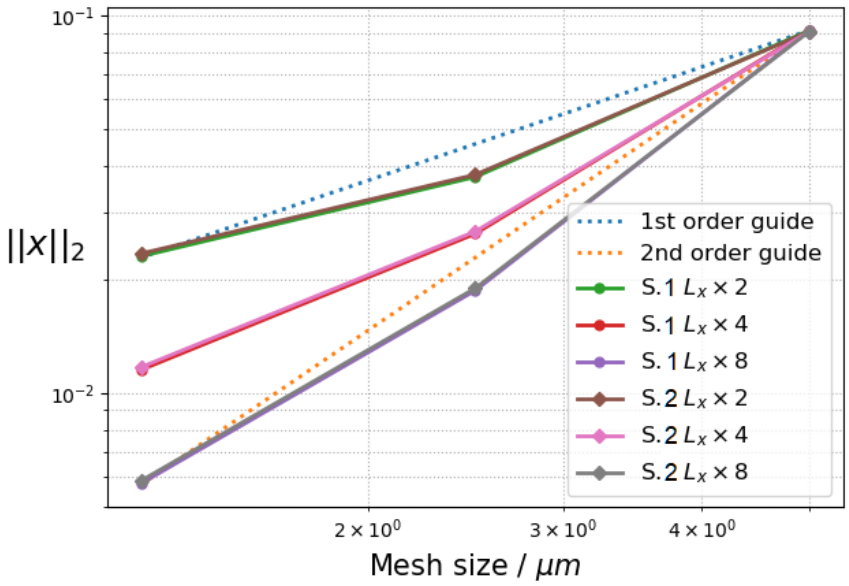

(a)

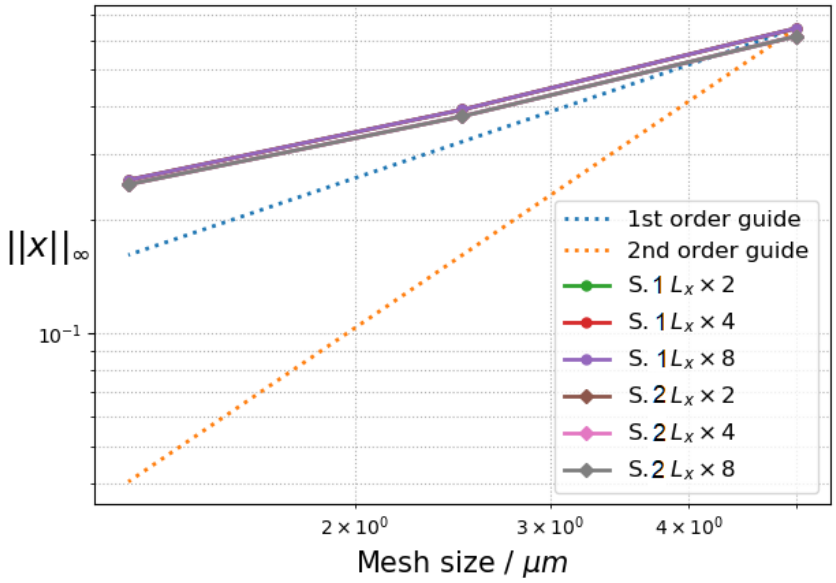

(b)

Figure 4.2: Euclidean (a) and maximum norm (b) of difference between numerical and analytic solution. Dashed lines offers as guide lines as they vary proportionally to mesh size in first and second order, respectively. Solid lines with dots denote error of stencil 1 and with diamonds imply error of stencil 2. Also, extending width of simulation domain by two-, four- and eight-fold are plotted with different colors, which is introduced as compensation for side reflection.

$$\begin{aligned}\psi(x,z) &= \frac{q(0)}{q(z)} exp\Big(-ik\frac{x^2}{2q(z)}\Big) \\ &= \frac{q(0)}{q(z)} exp\Big(\frac{}{18} ik\frac{x^2}{2R(z)} - \frac{x^2}{w^2(z)}\Big)\end{aligned} \tag{4.4}$$

Here, complex quantity $q(z)$ is introduced, defined with $R(z)$, wave's radius of curvature at location z, and $w(z)$, wave's spot size at location z by

$$\frac{1}{q(z)} \equiv \frac{1}{R(z)} - i\frac{\lambda}{\pi w^2(z)},$$
$$q(z) = z + i\frac{\pi w_0^2}{\lambda} = z + iz_R.$$

$z_R = \pi w_0^2/\lambda$ is termed Rayleigh range and $\phi = \tan^{-1}\lambda z/\pi w_0^2$ called Guoy phase [2].

Figure 4.3 provides a sketch of a gaussian beam passing through free space. With wavelength and spot size of wave at origin, one can easily describe the field profile along a gaussian beam referring to equation (4.4).

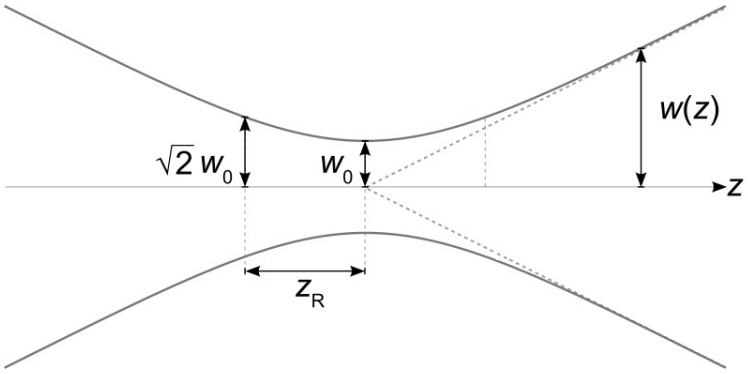

Figure 4.3: An illustration of a gaussian beam in free space.

Based on the stable solution of gaussian fundamental mode through free space given above, we can deduct a description for beams propagating in so-called gaussian ducts. A duct is an inhomogeneous medium where RI varies transversely in the way

$$n(x) = n_0 - \frac{1}{2}n_2x^2. \tag{4.5}$$

It is seen that RI depends on the location in x direction, reaching its peak at $x = 0$ and dropping quadratically with distance to z axis. Figure 4.4 depicts how RI changes in a duct with location.

The analytic solution for the Gaussian beam propagation in ducts is expressed as [2]

$$\psi(x,z) = \psi_0 \cdot exp\big(-\frac{x^2}{w_1^2} + i\frac{\bar{\lambda}z}{w_1^2}\big) \tag{4.6}$$

defining a steady-state spot size w_1 by

$$w_1^2 = \frac{\bar{\lambda}}{\pi\sqrt{n_2}}. \tag{4.7}$$

$\bar{\lambda}$ is the average wavelength in medium, i.e. $\bar{\lambda} = \lambda_0/\bar{n}$, and ψ_0 denotes amplitude of wave.

It describes a stable trapped gaussian eigenmode in a duct. The ideal shaped beam would be straight without spreading. However, if a gaussian beam that enters the duct characterized with unmatched shape, i.e., $w_0 \neq w_1$, oscillation ($w_0 < w_1$) or scalloping ($w_0 > w_1$) of beams take place in the duct. Before simulation, a matched spot size is calculated based on RI spread in the duct, and assigned to input continuous gaussian beam. Table 4.2 shows all parameters necessary for simulation.

To give an insight of shaping effect due to varying RI, spatial profiles of electric amplitude at different z locations are plotted in figure 4.5 (a) and (b) for stencil 1 and 2 respectively. As comparison, spatial profiles of gaussian beams through a uniform media are presented at the bottom row with (c) and (d) for two numerical results. Dashed lines near bottom of graphs mark positions determining spot size of different spatial profile, where the electric amplitude drops by $1/e^2$ compared to peaks. Note that all graphs are

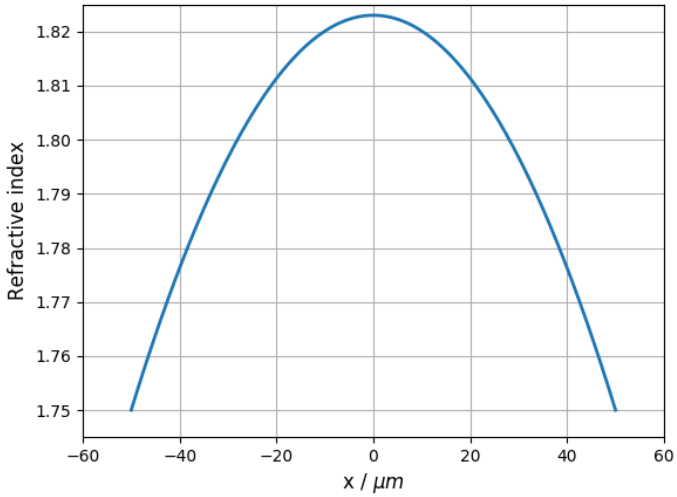

Figure 4.4: Profile of RI varying with x location in a duct.

Table 4.2: Parameters applied in simulation of gaussian beams through a duct

Description	**Symbol**	**Value**	**Units**
Length of simulation domain	L	100	μm
Initial Width of simulation domain	L_x	100	μm
Refractive index at origin	n_0	1.823	
Refractive index varying quantity	n_2	5.840×10^7	
Wavelength in free-space	λ_0	1	μm
Simulation duration	T	20	ps
Spot size of gaussian beams at origin	w_1	6	μm

plotted in the range between 40 μm and 60 μm in x direction to offer more legible presentation regarding spot sizes.

Table 4.3 gives accurate data of spot sizes at distinctive z locations. In the uniform medium, an obvious divergence of beam is observed as the beam spot size increases by around 0.6 μm with initial value of 6.00 μm. In contrast, beam spot size appears more stable in the duct, where it decreases by 0.2 μ m in simulation of stencil 1 whilst it stabilizes at 6 μm with fluctuation of $\pm$ 0.07 μm in simulation of stencil 2. The inaccuracy might be caused by assigning average RI in constitution of mesh grid. But in general, the results prove the shaping effect of a duct and validate the analytic solution of matched beam waist. Also, we can conclude that the stencil 2 simulates this scenario better than the stencil 1 in that spatial profile (a) shows evident decrease of peaks compared with (b).

4.3 Amplification of beams and pulses

The previous sections discuss about propagation of gaussian beams in either a uniform or an inhomogeneous medium. In both cases, neither loss nor gain is considered, which implies both RI and wave number k are real numbers. In this section, we are interested in a homogeneous medium with initial population of inversion, bringing gain to waves passing through it. Here three types of seeds are injected into simulation regime: continuous waves (CWs), square and Lorentzian pulses. Integral of electric field is conducted at the end of regime over space to calculate amplification of power and then compared to theoretical values and numerical calculation by Frantz-Nodvik model [3].

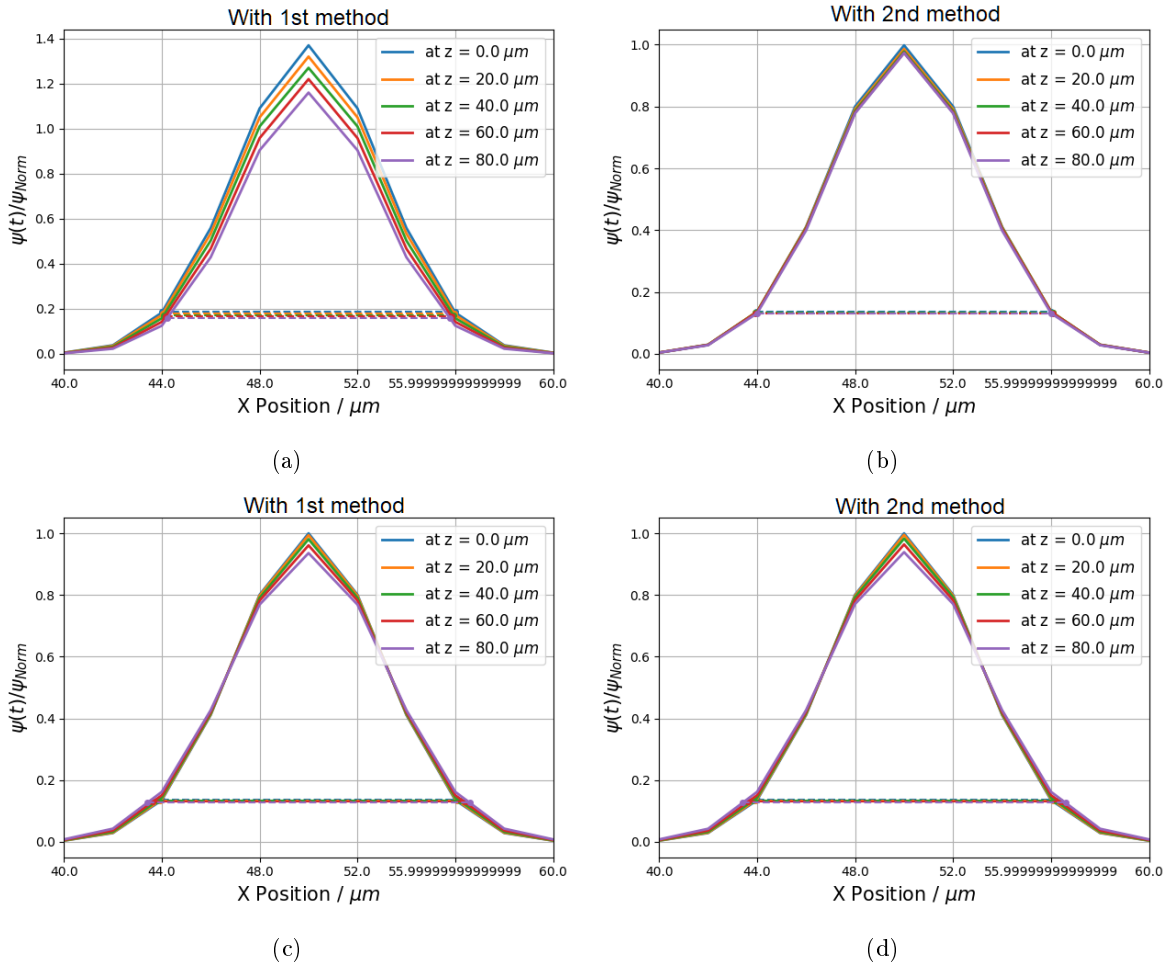

Figure 4.5: Spatial amplitude profile of continuous gaussian beams in a duct by stencil 1 (a) and 2 (b); figure (c) and (d) demonstrate results of gaussian beams through an uniform medium. Solid lines with different color indicate profile at different location in z direction, while dashed at bottom annotate spot size of corresponding profile. For a clearer comparison, all graphs are zoomed in to the range between $40\mu m$ and $60\mu m$.

Parameters concerning medium and seed injection are listed in the table below:

Referring to the equation (2.16), the theoretical gain of a plane CW can be easily known. The gain model established in last chapter enables simulation of CWs with a set of different mesh sizes. Figure 4.6 presents output of CWs at the end of simulation regime offered by three numerical methods. By comparing numerical and analytic results we can acquire relative error for each method, from which their pros and cons can be revealed. Table 4.5 lists the relative error with five mesh sizes. Two TDBPM methods reach much lower error compared to Frantz-Nodvik model, and the stencil 2 achieves the lowest among the three, allowing to constitute a sparse mesh grid to save computational expense within acceptable inaccuracy.

Besides plane CWs, Square and Lorentzian pulses are successively investigated, considering availability of the analytic solutions deducted in this paper [3] by Frantz and Nodvik. A square-shaped pulse can be described by the equation set

$$\psi(t) = \begin{cases} \psi_0 & 0 \leq t - z/c \leq p \\ 0 & \text{otherwise.} \end{cases} \tag{4.8}$$

Table 4.3: Spot sizes $w(z)$ of gaussian beams with $w_0 = 6\mu m$. Unit: μm

	Duct		**Uniform**	
	stencil 1	stencil 2	stencil 1	stencil 2
$z =$				
0	5.99	6.02	6.00	6.00
20	5.96	6.07	6.06	6.06
40	5.92	6.07	6.19	6.18
60	5.86	6.06	6.37	6.36
80	5.79	5.99	6.59	6.58

Table 4.4: Parameters applied in gain models

Description	**Symbol**	**Value**	**Units**
Length of simulation domain	L	1	cm
Initial Width of simulation domain	L_x	100	μm
Real refractive index	n_R	1.823	
Group refractive index	n_g	1.823	
Wavelength in free-space	λ_0	1	μm
Simulation duration	T	1	ns
Pulse duration of Lorentzian pulse	p	0.01	ns
Population inversion	Δ_0	8×10^{17}	cm^{-3}
Cross section of emission	σ_e	2.5×10^{-16}	mm^2
Initial Electric field	ψ_0	1×10^8	V/m

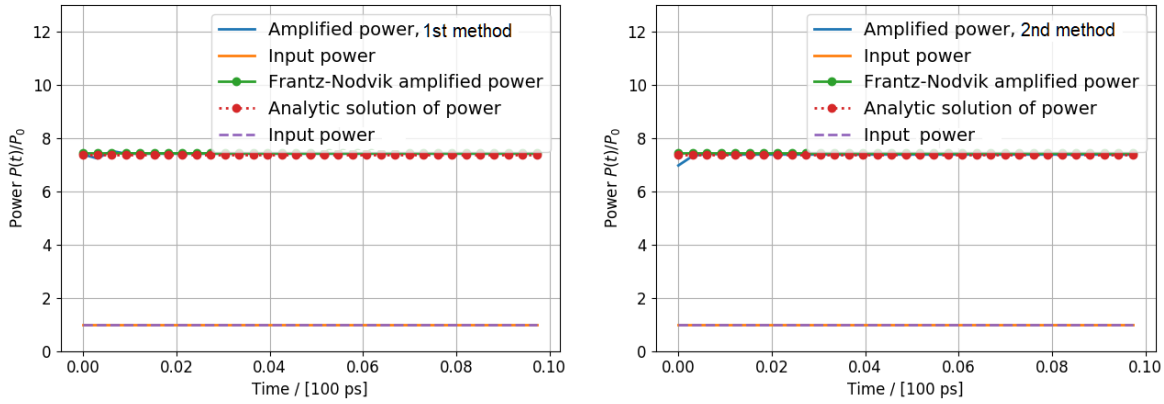

(a) (b)

Figure 4.6: Illustration of CWs simulated by stencil 1(a) and 2(b), compared to analytic and Frantz-Nodvik solutions.

while a Lorentzian time-dependent pulse corresponds to

$$\psi_0(t) = \frac{\psi_0 pT/\pi}{t^2 + T^2}. \tag{4.9}$$

Figure 4.7 and 4.8 demonstrate temporally varying output of square and Lorentzian pulses, respectively.

Table 4.5: Comparison of numerical calculation and theoretical solution

Mesh size / μm	**Stencil 1**	**Stencil 2**	**1D Model**
1000	7.978	0.167	26.041
500	4.167	0.042	11.317
200	1.705	0.007	4.196
100	0.859	0.002	2.048
20	0.173	0.010	0.402

Similarly, analytic solution and 1D model [6] are plotted as well as references. For better legibility the horizontal axis is limited within a short duration, when the most of interest parts appear.

In the scenario of square pulses, the preceding wave train is presented, showing fluctuation due to discontinuity as injected into the medium, and a distortion of pulse shape due to restricted population inversion. Table 4.6 offers a more clear comparison of three numerical methods. A different conclusion is arrived that 1D model achieves the lowest deviation; the difference between two TDBPM methods is quite narrow. Yet there is a huge difference in terms of two criteria, $\| x \|_2$ and $\| x \|_{max}$, where inaccuracy in the latter equals to ten times of the former and meanwhile barely drops with smaller mesh size. This phenomena and the abnormal figures with 20 μm mesh size may be the result of numerical discontinuity.

In this respect, the flat shape of Lorentzian pulse can to some degree avoid such disturbance. It is observed that fluctuations at beginning of the output are notably milder. Still, a similar conclusion is drawn according to the table 4.7 that 1D model achieves the most accurate solution to the theory, and distinction between two TDBPM is small as well. Further observation of two criteria leads to an improvement of accuracy with $\| x \|_{max}$, which yields greater error than values with $\| x \|_2$ yet in the same order of magnitude.

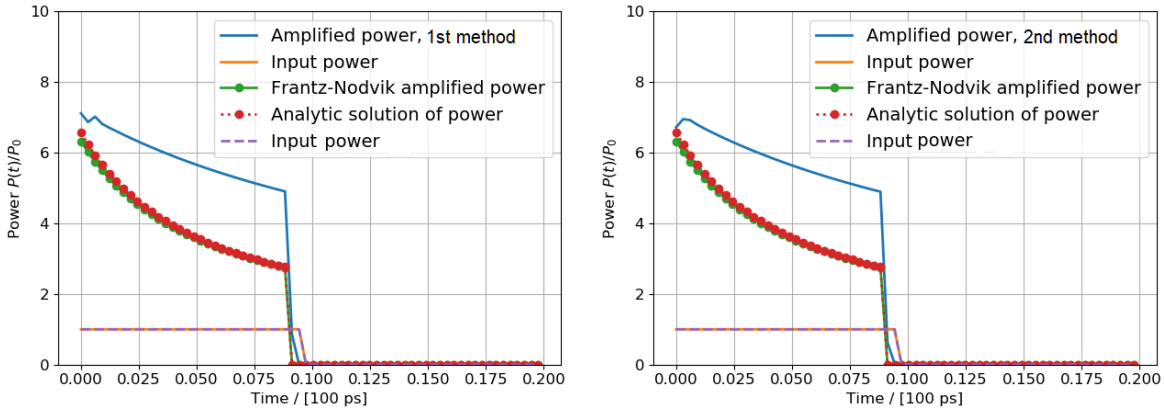

(a) (b)

Figure 4.7: Comparison of amplified square pulses calculated by stencil 1(a) and 2(b); mesh size is equal to 50 μm.

4.4 conclusion

In this chapter, convergence tests are conducted via simulation of continuous gaussian beams to validate stencil 1 and 2. By simulating gaussian beams in duct and amplification of beams as well as pulses, we can see a superior accuracy achieved by stencil 2. When amplification is taken into consideration, 1D model suits scenarios where computational expense is to be saved. However, 1D model fails to provide spatial information except in propagation direction, which stencil 1 and 2 preserve. Therefore, if spatial profile is of interest, stencil 1 and 2 should be incorporated.

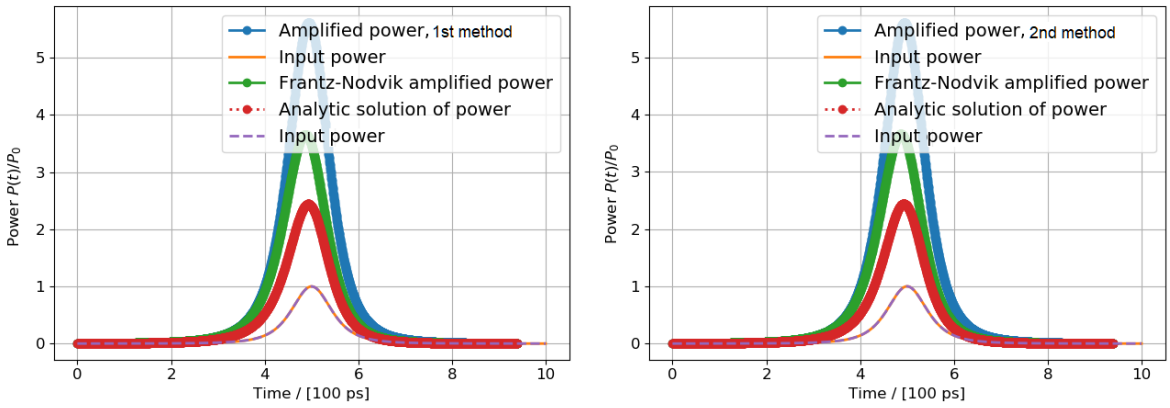

(a) (b)

Figure 4.8: Comparison of amplified Lorentzian pulses calculated by stencil 1(a) and 2(b), where mesh size equals to 50 μm.

Table 4.6: Table of error in square pulses

Mesh size / μm	**Stencil 1**		**Stencil 2**		**1D Model**	
	$\| x \|_2$	$\| x \|_\infty$	$\| x \|_2$	$\| x \|_\infty$	$\| x \|_2$	$\| x \|_\infty$
1000	0.440	4.994	0.427	5.052	0.230	2.916
500	0.337	4.998	0.321	4.894	0.122	2.098
200	0.253	5.003	0.244	4.770	0.050	1.165
100	0.218	5.006	0.213	4.723	0.025	0.675
20	0.316	11.46	0.290	11.526	0.005	0.156

Table 4.7: Table of error in Lorentzian pulses

Mesh size / μm	**Stencil 1**		**Stencil 2**		**1D Model**	
	$\| x \|_2$	$\| x \|_\infty$	$\| x \|_2$	$\| x \|_\infty$	$\| x \|_2$	$\| x \|_\infty$
1000	0.109	0.358	0.128	0.447	0.029	0.051
500	0.116	0.393	0.126	0.439	0.025	0.045
200	0.120	0.415	0.124	0.434	0.023	0.042
100	0.121	0.423	0.123	0.433	0.022	0.041
20	0.129	0.440	0.130	0.442	0.021	0.040

Bibliography

[1] B. Berneker, *Dynamische Simulation von Halbleiterlasern basierend auf neuartigen Finiten Elelmenten*. PhD thesis, Universität Erlangen-Nürnberg, 2010.

[2] A. E. Siegman, *Lasers*. University Science Books, 1986.

[3] L. M. Frantz and J. S. Nodvik, "Theory of pulse propagation in a laser amplifier," *Journal of Applied Physics*, vol. 34, no. 8, pp. 2346–2349, 1963.

[4] M. Wohlmuth, *Modeling and Simulation of Solid-State Laser Resonators Using a Dynamic Multimode Analysis(DMA)*. PhD thesis, Universität Erlangen-Nürnberg, 2012.

[5] O. Svelto and D. C. D. C. Hanna, *Principles of lasers*. Plenum Press, 1998.

[6] X. Rao, R. Springer, and C. Pflaum, "Simulation of Pulse Amplification in Three Dimensions," 2018.